Environ Fluid Mech (2014) 14:873–893
DOI 10.1007/s10652-013-9328-x

ORIGINAL ARTICLE

Experimental and large eddy simulation study of the flow developed by a sequence of lateral obstacles

W. Brevis · M. García-Villalba · Y. Niño

Received: 13 April 2013 / Accepted: 1 December 2013 / Published online: 10 January 2014

Abstract In this paper we provide a description of the three-dimensional flow induced by a sequence of lateral obstacles in a straight shallow open-channel flow with flat bathymetry. The obstacles are modelled as rectangular blocks and are located at one channel wall, perpendicular to the main stream direction. Two aspect ratios of the resulting dead zones are analysed. The flow structure is experimentally characterised by particle image velocimetry measurements in a laboratory flume and simulated using three-dimensional Large Eddy Simulations. Good agreement between experimental measurements and numerical results is obtained. The results show that the effect of the obstacles in the main channel is observed up to one obstacle length in the spanwise direction. The spacing between obstacles does not seem to have a large influence in the outer flow. The mean flow within the dead zone is characterised by a large recirculation region and several additional vortex systems. They are discussed in the paper, as well as the mean and root-mean-square wall shear-stresses.

Keywords Dead zones · Particle image velocimetry · Large eddy simulation · Shallow flow · Groyne fields

1 Introduction

Due to the important role that they play in several processes and mass transport in fluvial systems, in recent years, there has been a renewed interest on improving the understanding of

W. Brevis (✉)
Structural and Civil Engineering Department, University of Sheffield, Sir Frederick Mappin Building, Mappin Street, Sheffield S1 3JD, UK
e-mail: w.brevis@sheffield.ac.uk

M. García-Villalba
Universidad Carlos III de Madrid, Bioingeniería e Ingeniería Aeroespacial, Leganés 28911, Madrid, Spain

Y. Niño
Civil Engineering Department and Advanced Mining Technology Centre, University of Chile, Blanco Encalada 2002, Santiago, Chile

the flow physics associated to open channel dead zones (DZ). DZ can be defined as large scale recirculating volumes of water that are stagnant compared with a faster flow occurring in an adjacent main stream. These zones can be generated by natural morphological changes [10] or by the presence of hydraulic structures. Due to the low velocities and high retention times within DZ, several fluvial processes can be affected. Some examples are the modification of the sediment budget due to large sedimentation rates of particulate material [13], changes on the transport of dissolved substances due to an increased longitudinal dispersion [26,28], and also the generation of improved hydrodynamics conditions for flora and fauna [21]. An improved understanding of three-dimensional physical mechanisms governing the mass exchange and turbulence at the interfacial region and within dead zones is important to build design rules according to engineering and ecological requirements.

Dead zones can be formed as a result of the presence of emergent and submerged structures. Depending on the case, DZ are termed here as emerged DZ and submerged DZ. Based on their geometrical layout DZ can be also classified into single DZ and DZ sequence [3]. In case of single DZ, the interfacial flow between DZ and the main stream is developed locally. In DZ sequence the interface is the result of the superposition of the locally developed interfacial structure and the flow resulting from upstream DZ's. The present work deals with emerged DZ in a sequence. For simplicity, we consider the DZ sequence generated by a series of obstacles with a rectangular geometry. Similar geometries can be found in most human made DZ such as the ones formed in groyne fields and in-stream structures for river restoration projects.

The flow structure in an emerged rectangular DZ is mainly determined by its aspect ratio, λ, which is defined as the ratio between its streamwise, W, and spanwise, L, dimensions, $\lambda = W/L$, [23,26] (see Fig. 2 below). The flow can be composed by one or more gyres of vertical axis, which are driven by a shear structure developed at the interface with the main channel [22,26]. The gyres cover a large region within the DZ. However, the interfacial shear layer and the impingement of the flow against the downstream obstacle are the main responsible for the mass and momentum exchange with the adjacent main stream [6,26]. The shear layer controls the mass exchange through the dynamics of a complex set of vortical patterns. When these structures are transported, they can hit the downstream corner of the DZ surrounding fluid from the main channel which is incorporated into the dead zone (engulfing process) [17]. For illustration, Fig. 1 shows one of our preliminary experimental flow visualizations of the shear layer, its impingement against the downstream obstacle, and the resulting wall-attached jet-like flow, for two aspect ratios. Most of the known aspects of the flow in DZ have been obtained in studies aimed at the understanding of their mass exchange dynamics with the main channel. Due to the fact that in shalllow conditions the exchange process and residence

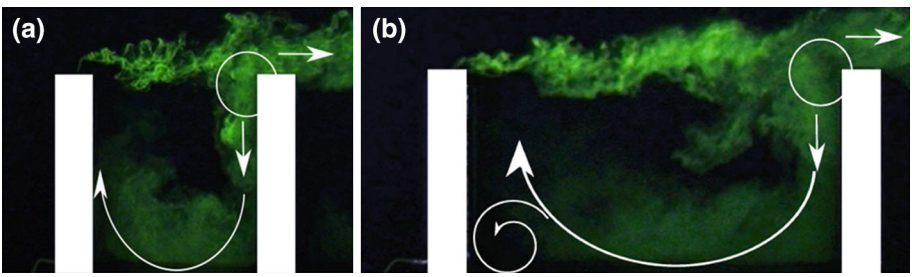

Fig. 1 **a** Flow visualisation for $\lambda = 1$. **b** Flow visualisation for $\lambda = 2$

times are mainly governed by large-scale quasi two-dimensional flow structures, most of previous experimental researches have been based on two-dimensional surface measurements [6,26,28]. One limitation of these approaches is that they cannot provide information of the the vertical changes of the flow structure and the magnitude of wall shear stresses, which can be important to improve the engineering and ecological design of DZ.

Two of the works providing information about the vertical flow structure of DZ are those of Sukhodolov et al. [23] and McCoy et al. [17]. Based on field pointwise measurements in emerged groyne fields, Sukhodolov et al. [23] showed that the mean velocity field within a DZ remains almost constant with depth, i.e. the mean field can be characterized as quasi two-dimensional (Q2D). McCoy et al. [17] based on large eddy simulations (LES) of a groyne field sequence of $\lambda = 1.4$, reported that despite the fact that the flow inside the DZ can be characterized as Q2D, the interfacial flow in the shear layer region is heterogeneous in the vertical direction. They observed that a three-dimensional description of the flow in this area is essential to describe the mass exchange. Their simulations showed that most of the fluid leaves the dead zone via the interfacial top layer and enters the embayment region at levels situated around the mid-depth, practically over the whole length of the dead zone. One of the main characteristics of this work was the use of a variable bathymetry, which was composed by an sloped-bottom inside the cavity and a step at the interface of about 40 % of the water depth.

On the computational side, most previous numerical simulations have considered a single obstacle and only a few numerical works have contributed to the three-dimensional description of the flow in an obstacles sequence. Following the numerical simulations of McCoy et al. [17], Constantinescu et al. [6] performed LES of the mass exchange process between a sequence of groyne fields and main channel. Good agreement was found with the prediction of a morphometric exchange parameter proposed by Weitbrecht et al. [29]. Abad et al. [1] performed 3D RANS simulations of the flow around a sequence of groyne fields. The simulations and measurements presented by Abad et al. [1] are one of the few available for non-shallow conditions (The in-stream structures were aimed at the control of riverbank erosion). Hinterberger et al. [12] performed 3D LES and 2D-depth-averaged calculations of an obstacles sequence and obtained a good agreement with laboratory Particle Image Velocimetry measurements. They showed the over-estimation of the mass-exchange between DZ and main channel obtained by the depth-averaged simulations. Karami et al. [14] studied the sediment bed evolution in a sequence of two groyne fields using RNG $k - \varepsilon$ simulations. Sediment transport was simulated based on semi-empirical equations and the results showed good agreement with bathymetric laboratory measurements. Finally, Tritthart et al. [25] performed RANS calculations of a section of the Danube river in Austria. They obtained a good performance in terms of the estimation of residence time within the DZ. Tritthart et al. stressed the limitations of the RANS approach to capture the structure of the shear layer and recommended the use of Eddy resolving techniques for this purpose.

In the present work, we present a combined experimental and numerical study of shallow, open-channel flow in an emerged DZ sequence. The experiments and simulations are aimed at the characterization of the vertical flow structure for a DZ in a large sequence, where the interfacial flow is fully developed. As the influence of a complex bathymetry in the characteristics of the flow within DZ, interface and main channel is not fully understood, in this work a flat bathymetry is used. This is an important difference with respect to the study of McCoy et al. [17]. The paper starts with a description of the experiments and the LES. This is followed by a validation of the LES by comparison of the obtained results with the experimental data. Then, the vertical structure of the flow is studied and an estimation of the wall shear-stress is provided. Some final comments are provided in the conclusions.

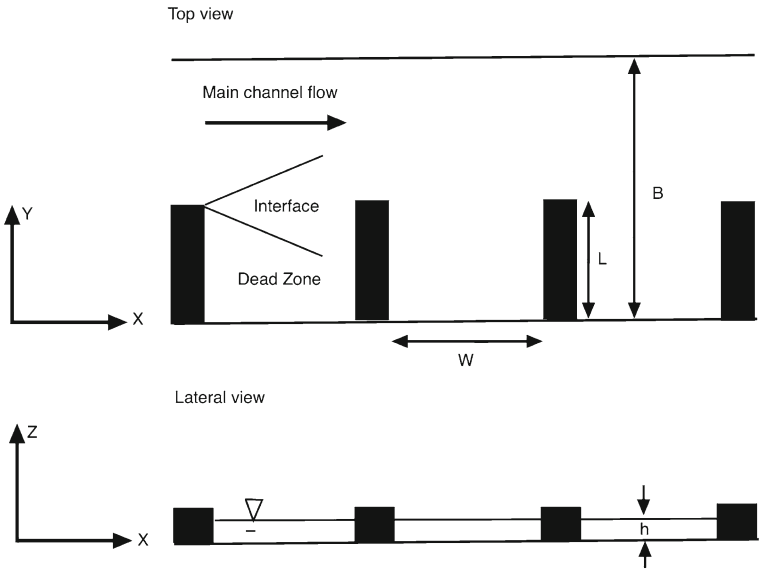

Fig. 2 Definition of geometrical parameters

2 Experiments description

The experiments were conducted in a 17 m long and 1.3 m wide, rectangular tilting flume at the Institute for Hydromechanics, Karlsruhe Institute of Technology (KIT). The longitudinal slope for the experiments was fixed to approximately S = 0.001 m/m. The flume bottom consisted of laminated plastic with small sand elements of diameter <0.002 m. The flume inflow was connected to a constant head tank and the flow rate controlled by an inductive flowmeter together with a computer-controlled gate valve. In order to avoid the formation of upstream perturbations, the flow was aligned by using honeycomb diffusers of about 0.2 m wide. The discharge was constant and equal to $Q = 0.00975\ \mathrm{m}^3/\mathrm{s}$, with a quasi-uniform water depth of $h = 0.07$ m at the measurement area. With this configuration the aspect ratio of the channel cross-section was set to $B/h \approx 18$, where B is the channel width, which according to Nezu & Rodi [18] is characterised by a multi-cellular array of secondary currents. The Reynolds number based on the channel bulk velocity $U = Q/(Bh) = 0.107$ m/s, and water depth, was $Re_h = hU/\nu = 7,500$. These flow conditions were selected in order to ensure a low Froude number, $Fr = U/\sqrt{gh} = 0.13$, and as a consequence almost no water surface fluctuation were observed. The obstacles were modelled by means of rectangular PVC blocks of $0.25 \times 0.075 \times 0.05\ \mathrm{m}^3$. The relation $B/L = 5.2$ was larger than real world configurations, but necessary to isolate the flow from additional effects caused by the interaction of the shear-layer, developed by the groyne sequence, with the opposite bank. Figure 2 shows the definition of the geometrical parameters used in this work.

The obstacles were placed over the whole length of the flume to ensure a fully developed horizontal shear layer in the interfacial region. The measurement area was located after approximately 20 DZ and about 10.5 m downstream the flume inlet and 6.5 m upstream the outlet. The length necessary for the full development of the boundary layer, L_δ, was estimated based on the relation proposed by Kirkgöz and Ardiçhoglu [15] for a smooth wall. This relation indicated a length $L_\delta = 5.3$ m, almost half the distance used in the present

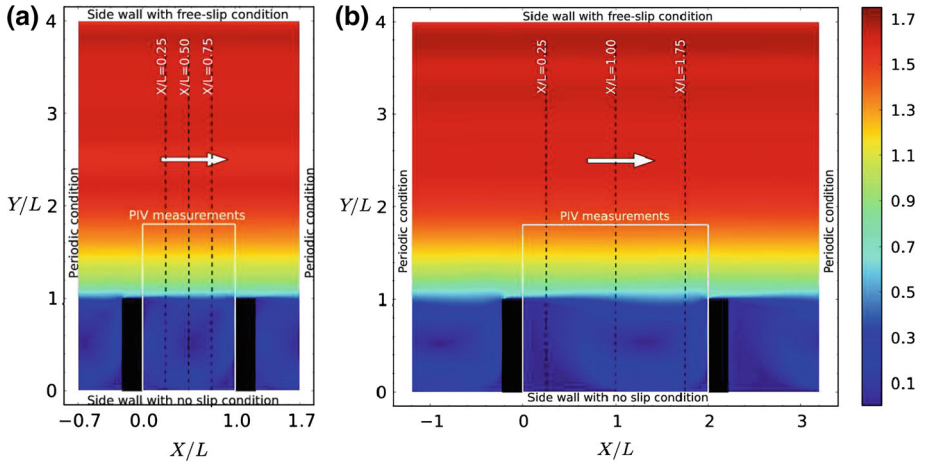

Fig. 3 Top view of the computational domain and boundary conditions for the simulations. The region where PIV measurements were taken is marked by the *white rectangle*. The *dashed lines* show the positions used for comparison between experimental and numerical results in Figs. 8, 9, 10, and 11. The *colour* indicates the magnitude of the mean velocity vector at $h/2$. **a** $\lambda = 1$. **b** $\lambda = 2$.

experimental setup. As a result of this analysis, the existence of a fully developed bottom boundary layer in the measurement area was assumed. In addition, and also according to Kirkgöz and Ardiçhoglu [15], the cross-sectional channel aspect ratio ensures that the bottom boundary layer was developed up to the free surface, at the channel centre line.

The bulk velocity U and the length of the obstacles, L, were used to normalise all flow quantities. In this work the streamwise, spanwise and vertical coordinates are denoted X, Y and Z. The corresponding instantaneous velocity components are denoted $u = \langle u \rangle + u'$, $v = \langle v \rangle + v'$ and $w = \langle w \rangle + w'$, where $\langle\rangle$ indicates a time-averaged quantity and $'$ a fluctuation with respect to the time-average.

2.1 Measurement technique

The velocity field was measured at the half-height of the channel, $h/2$, using particle image velocimetry (PIV). The region in which the PIV measurements were taken is marked with a white rectangle in Fig. 3. The flow was seeded with polyamide particles of 100 μm mean diameter and density 1.016 g/cm^3. The particles were illuminated by a dual-cavity Q-switched Nd:Yag laser of 532 nm and maximum energy output of 120 mJ per pulse. The horizontal laser plane was open from the channel side by using a conventional cylindrical lens. A CCD scientific camera of 1,280 × 1,024 pix, working at 5 Hz was used to record a top view of the flow. The camera was operated in double-frame mode with a time interval between each snapshot of 40 ms. The movement of the tracer particles was recorded for 10 min and the resulting 3,000 double-frame pictures were analysed using the PIV package for Linux GPIV and in-house Python algorithms. Multi-pass and image deformation [20] techniques were used during the analysis.

The PIV results were transformed from image coordinate (IC) to real world coordinates (RWC) using an image of a calibration grid which was carefully positioned in the measurement region by means of a computer controlled three-dimensional traverse system. The image was analysed using an in-house algorithm which makes use of a linear interpolation technique and a Delaunay triangulation approach to determine the relation between IC and

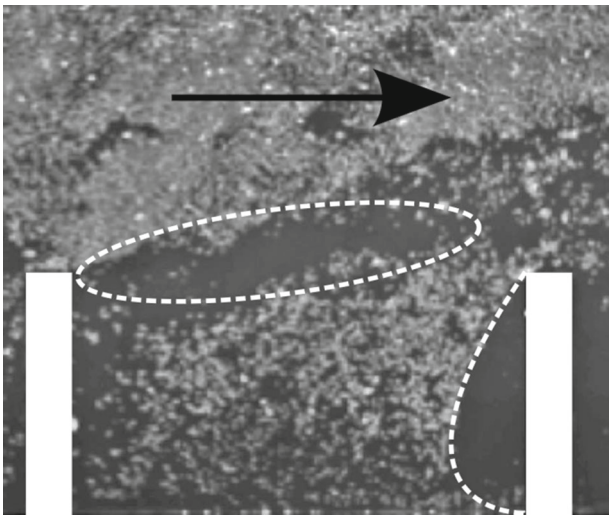

Fig. 4 Snapshot of water surface measurements showing presence of strong upwelling events in shear layer and impingement region, no particles can be observed in these regions (*dashed lines*). The *arrow* show the flow direction and the *white rectangles* the obstacle positions.

RWC. The use of this algorithm was introduced by Brevis and Garcia-Villalba for the calibration of visualisation images in shallow flows [4]. The calibrated results were filtered using an iterative implementation of the normalised median filter of Westerweel and Scarano [30] proposed by Brevis et al. [5].

Experiments at the water surface using floating tracers were also performed, however after the analysis of the images these data were discarded. The reason was that the flow at the water surface was characterised by intermittent upwelling events in the DZ and shear layer region. One of the most important issues regarding the use of floating tracer was the renewal of the water surface induced by the impingement of the shear layer against the downstream obstacle. The particles were literally washed-out from this region and no velocity information could be gathered during these events. The main implication of this is that only conditional-statistics can be obtained in that zone leading to a partial description of the flow. A snapshot of the seeded water surface is shown in Fig. 4 in which the problematic regions have been highlighted. This might be a severe limitation for this kind of measurements in shallow flows with obstacles sequences as the present one.

3 Computational approach

The calculations were performed with the in-house code LESOCC2 [11], which is a successor of the code LESOCC developed by Breuer and Rodi [2]. The code solves the Navier-Stokes equations on body-fitted, curvilinear grids using a cell-centred finite volume method with collocated storage. Second order central differences are employed for both the convection and diffusive terms. The time integration is performed with a predictor-corrector scheme, where the explicit predictor step for the momentum equations is a low-storage three-step Runge–Kutta method. The corrector step covers the implicit solution of the Poisson equation for the pressure correction.

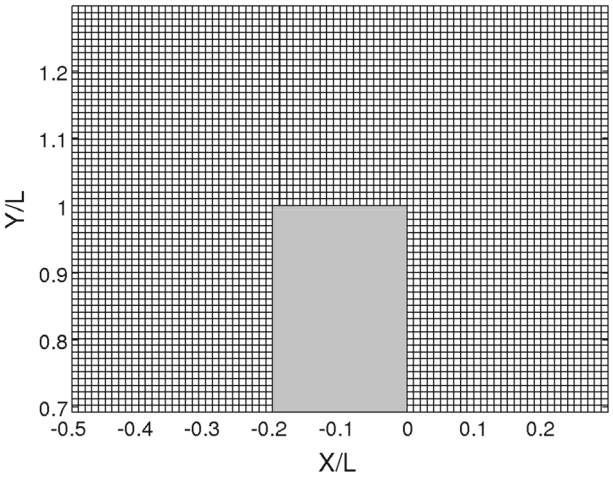

Fig. 5 View of the grid in a *horizontal plane* in the region near the structure tip

The subgrid-scale (SGS) stresses, resulting from the unresolved motions, are modelled using the dynamic Smagorinsky subgrid-scale model, first proposed by Germano et al.[9] and subsequently modified by Lilly [16]. In the dynamic procedure, the parameter of the model is determined using an explicit box filter of width equal to twice the mesh size and smoothed by means of temporal under-relaxation [2]. Furthermore, the subgrid-scale viscosity was clipped to avoid negative values. This method has been succesfully used for other complex flows [7,8,19].

The configuration studied consists of the shallow flow around a periodic sequence of obstacles, as shown in Fig. 3. In the present simulations two obstacles were included in the calculation. The length, width and height of each obstacle are $L, d = 0.2\ L$ and $h = 0.28\ L$, respectively. The distance between two obstacles is W. Two cases have been considered, a case with aspect ratio $\lambda = 1$, in which $W = L$ and a case of aspect ratio $\lambda = 2$, in which $W = 2L$. The size of the computational domain is $(2W + 2d) \times 4L \times h$ in streamwise, spanwise and wall-normal directions, respectively. As in the experiment the Reynolds number based on the bulk velocity U and the water depth h, $Re = Uh/\nu$, was 7,500, which ensured a fully turbulent flow within and outside the DZ.

The numerical mesh in case $\lambda = 1$ ($\lambda = 2$) contains 240(440) $\times$ 400 $\times$ 70 cells in streamwise, spanwise and wall-normal directions, respectively. The grid is equidistant in the three directions, with the same cell size in x and y directions and a smaller cell size in z direction. The aspect ratio of the cell is roughly 3, which is considered a reasonable number. A zoom of the region near the tip of the structure is shown in Fig. 5 to provide a visual impression of the grid resolution. In terms of the friction velocity in the main stream, grid spacings in streamwise and spanwise direction are $\Delta x^+ = \Delta y^+ \simeq 18$. The grid spacing in the vertical direction is $\Delta z^+ = 6$. Therefore, the meshes employed are finer than those employed by Hinterberger et al. [12] for a similar configuration, especially in the vertical direction. The resolution employed is reasonable everywhere, as suggested by the comparisons shown in the next section, except near the downstrean obstacle where impingement occurs. In this zone further grid refinement would have been desirable to obtain a better flow representation.

Periodic boundary conditions were used in streamwise direction. No-slip conditions were used at the bottom wall and at the surfaces of the groynes. Free-slip conditions were used

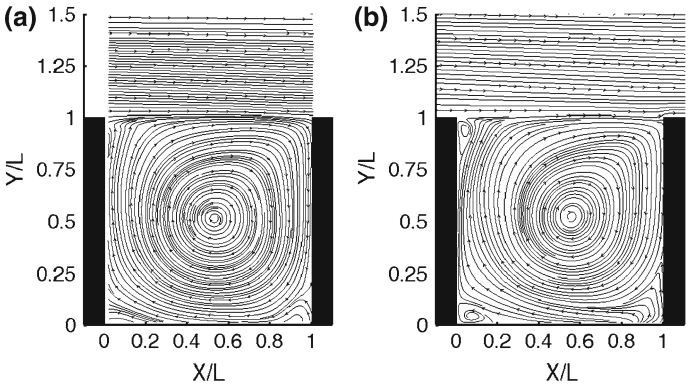

Fig. 6 Streamlines of the mean flow projected in a wall-parallel plane located at $Z = 0.5h$. Case $\lambda = 1$. **a** experiment, **b** simulation

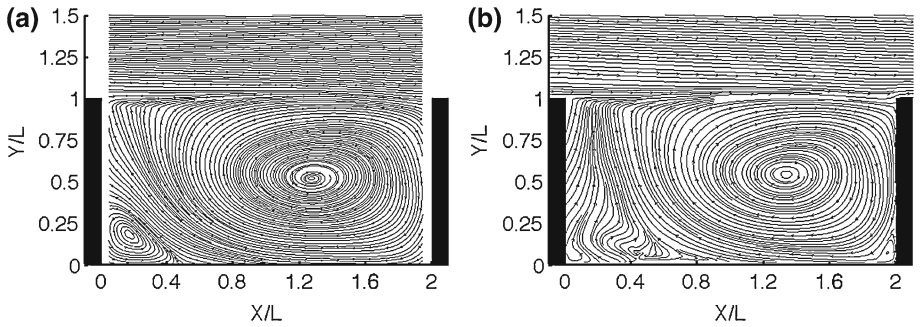

Fig. 7 Streamlines of the mean flow projected in a wall-parallel plane located at $Z/L = 0.14$. Case $\lambda = 2$. **a** experiment, **b** simulation

at the lateral wall and at the free-surface, the latter is therefore modelled using a rigid lid assumption. In the experiment, ultrasonic measurements of the water surface position showed no fluctuations, validating the rigid lid assumption for this configuration. In the simulations, after discarding initial transients, statistics were collected for a time period of approximately 300 L/U.

4 Results

4.1 Comparison between numerical simulations and experiments

In general a good agreement was found between simulations and experiments at half water depth. A qualitative comparison is provided in Figs. 6 and 7 for both cases $\lambda = 1$ and $\lambda = 2$. Figure 6 (Fig. 7) compares streamlines of the mean flow predicted by the simulation with the streamlines of the mean flow measured in the experiment for case $\lambda = 1$ ($\lambda = 2$). In both cases, the size and the shape of the main recirculation zone are equivalent in experiment and simulation. In case $\lambda = 1$ the main recirculation zone fills the whole DZ, and the eye of the recirculation zone is located roughly half-way between both obstacles. This is well predicted in the simulation. In case $\lambda = 2$ the eye of the main recirculation zone is displaced towards

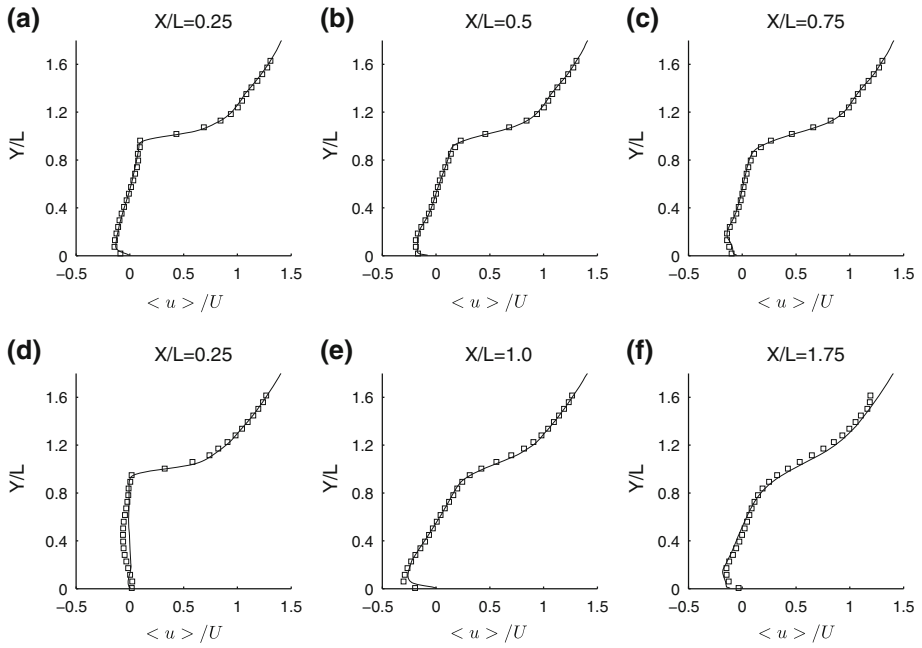

Fig. 8 Comparison between numerical results (*solid line*) and experimental measurements (*symbols*) for $\langle u \rangle / U$ at three X/L positions. **a**–**c** $\lambda = 1$, **a** $X/L = 0.25$, **b** $X/L = 0.5$, **c** $X/L = 0.75$. **d**–**f** $\lambda = 2$, **d** $X/L = 0.25$, **e** $X/L = 1$, **f** $X/L = 1.75$

the downstream obstacle, a feature also captured in the simulation. Also for case $\lambda = 2$, a secondary recirculation in the lee of the upstream obstacle is observed in the experiment, (Fig. 7a). This secondary recirculation region is not observed in the simulation data (Fig. 7b). It should be mentioned that in the simulations of Hinterberger et al. [12], corresponding to the experiments of Weitbrecht [27], a similar lack of agreement for this secondary recirculation zone was observed. Among the possible explanations for this discrepancy, Hinterberger et al. mention the coarse resolution in vertical direction in their study. In the present case, the resolution in vertical direction is significantly better (70 grid points in this study versus 15 grid points in [12]), however, the secondary recirculation region still does not form. Therefore, there might be other explanations for this discrepancy, and this issue deserves further investigation.

A quantitative comparison between experiments and simulations is provided in Figs. 8, 9, 10, and 11. For each case, measurements and numerical results are presented at mid-height, at three streamwise locations (as displayed by dashed lines in Fig. 3), as a function of the spanwise coordinate Y/L. Two of the streamwise locations correspond to the lee of the upstream obstacle and to the front of the downstream obstacle (both at a distance of 0.25 L to the corresponding obstacle). The third location corresponds to half-way between the obstacles, i.e. a distance of $0.5L$ (L) in case $\lambda = 1$ ($\lambda = 2$).

Figure 8 displays the comparison for the mean streamwise velocity component. The agreement between experimental data and numerical results is very good for both cases at all three locations. The profiles do not differ much from case $\lambda = 1$ to $\lambda = 2$. For example, at $Z/L = 0.14$ (half-depth), the magnitude of the backflow inside the dead zone is comparable in both cases, reaching a value of 0.25 U near the lateral wall (around $Y/L \sim 0.1 - 0.2$). The

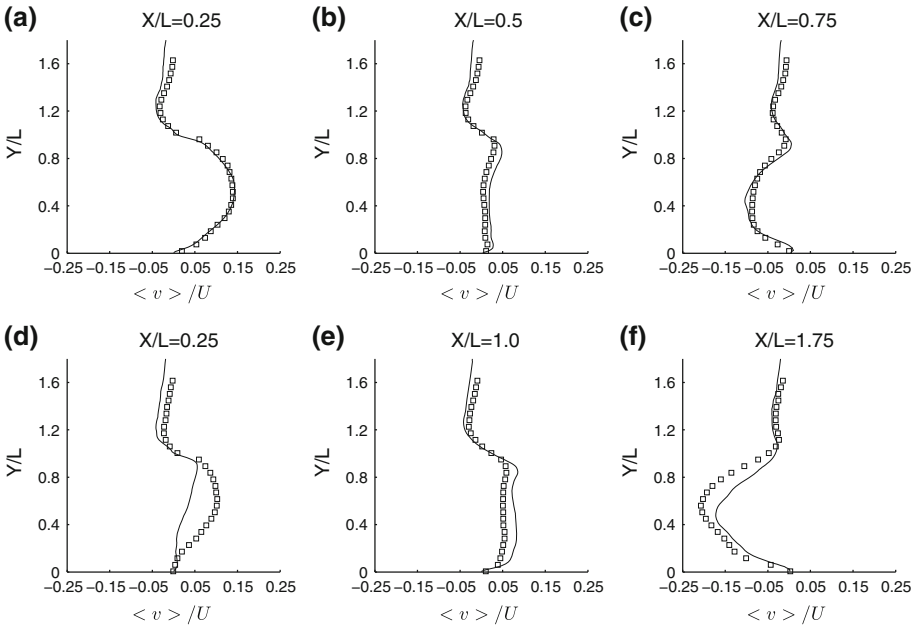

Fig. 9 Comparison between numerical results (*solid line*) and experimental measurements (*symbols*) for $\langle v \rangle / U$ at three X/L positions. **a**–**c** $\lambda = 1$, **a** $X/L = 0.25$, **b** $X/L = 0.5$, **c** $X/L = 0.75$. **d**–**f** $\lambda = 2$, **d** $X/L = 0.25$, **e** $X/L = 1$, **f** $X/L = 1.75$.

shear layer that develops between the dead zone and the main stream presents two distinct regions. In the range $1 < Y/L < 1.2$ the gradient is steeper than further outwards. This effect is somewhat stronger in case $\lambda = 1$ than in case $\lambda = 2$, as can be observed from the corresponding plots near the downstream obstacle, (Fig. 8c in case $\lambda = 1$ and Fig. 8f in case $\lambda = 2$). For $Y/L > 1.2$, the slope of the profiles is milder until a uniform stream is reached in both cases $\lambda = 1$ and $\lambda = 2$, approximately at $Y/L \sim 2$ (not shown in the figures).

The comparison for the mean spanwise velocity $\langle v \rangle$ component is shown in Fig. 9. For this quantity, the agreement between experiments and calculations is better in case $\lambda = 1$ than in case $\lambda = 2$. This result confirms the qualitative observation of the streamlines plots displayed in Figs. 6 and 7 discussed above. In case $\lambda = 1$ the agreement is fairly good at the three locations. In the dead zone, the maximum value is in the range $\langle v \rangle / U \sim 0.1$–$0.15$ and occurs at mid span. The value of $\langle v \rangle / U$ in the outer zone, $Y/L > 1$, is small. In case $\lambda = 2$ the agreement is satisfactory at $X/L = 1$ and $x/L = 1.75$. However, the agreement is not good for the profile at $X/L = 0.25$, corresponding to the lack of the secondary gyre in the simulation.

Second-order statistics are compared in Fig. 10, $\langle u'u' \rangle$, and Fig. 11, $\langle u'v' \rangle$. Profiles of $\langle v'v' \rangle$ are not shown, but the trend of the agreement between experiment and simulation is similar as for $\langle u'u' \rangle$. For the latter quantity, the agreement is fairly good at all three locations for both cases. In case $\lambda = 1$, the level of fluctuations appears to be negligible in the DZ. Then, there is a pronounced peak in the shear layer that is formed between the dead zone and the main stream, in the range $1 < Y/L < 1.2$, which corresponds well with the region with the steeper spanwise gradient of $\langle u \rangle$, Fig. 8**a**–**c**. The magnitude of the peak appears to be slightly underpredicted in the simulation. This is clearly seen in Fig. 10b–c. The longitudinal

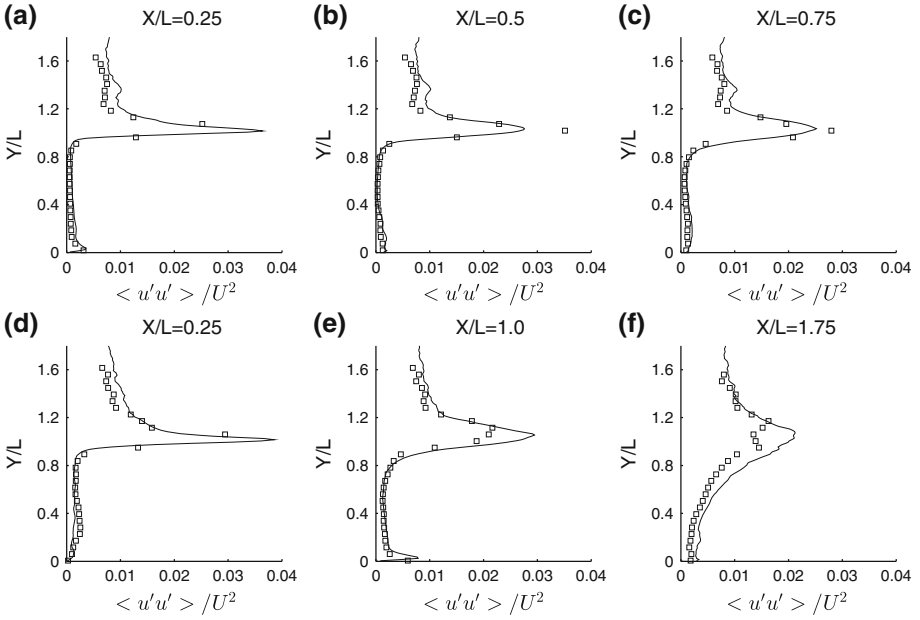

Fig. 10 Comparison between numerical results (*solid line*) and experimental measurements (*symbols*) for $\langle u'u' \rangle / U^2$ at three X/L positions. **a–c** $\lambda = 1$, **a** $X/L = 0.25$, **b** $X/L = 0.5$, **c** $X/L = 0.75$. **d–f** $\lambda = 2$, **d** $X/L = 0.25$, **e** $X/L = 1$, **f** $X/L = 1.75$.

development of the shear layer can be observed by the widening of the peak, it is very thin in the lee of the upstream obstacle and widens with increasing X. Beyond $Y/L = 1.2$, $\langle u'u' \rangle$ presents smaller values. Beyond $Y/L = 2$ (not shown in the figures) the level of fluctuations correspond to the one observed in an unperturbed straight channel flow.

In case $\lambda = 2$, the profiles present similar features as in case $\lambda = 1$ but with some differences. For this case, the simulation slightly overpredicts the peak of $\langle u'u' \rangle$. The shear layer in case $\lambda = 2$ has more length to develop, since the distance between two consecutive obstacles is double. Therefore the peak broadens more than in case $\lambda = 1$. The turbulent activity within the dead zone is also clearly larger than in case $\lambda = 1$; it is larger the closer the location to the downstream obstacle. For example at $X/L = 1$, (Fig. 10e), values of $\langle u'u' \rangle \sim 0.002U^2$ in the whole dead zone are obtained. Significantly larger values are observed at $X/L = 1.75$, (Fig. 10f). Such large values are not seen near the downstream obstacle in case $\lambda = 1$, (Fig. 10c). In the outer region, beyond $Y/L = 1.5$ the level of fluctuations is comparable between cases $\lambda = 1$ and $\lambda = 2$. Therefore, it might be concluded that for the turbulence in the outer stream, it does not make much difference the spacing between the obstacles, while for the turbulence in the interior of the dead zone the distance between obstacles is a critical parameter.

Finally, the agreement for the shear stress $\langle u'v' \rangle$ between experiment and simulation is also good (Fig. 11). The magnitude, location and shape of the peak is well predicted for both cases $\lambda = 1$ and $\lambda = 2$, with a small overprediction in case $\lambda = 2$ at the two downstream locations, (Fig. 11**e**–**f**).

The comparisons shown in this section lead us to the conclusion that the simulations predict well the mean flow and turbulent structure in both cases, with the exception of the mean secondary flow in the lee of the upstream obstacle for case $\lambda = 2$. The information

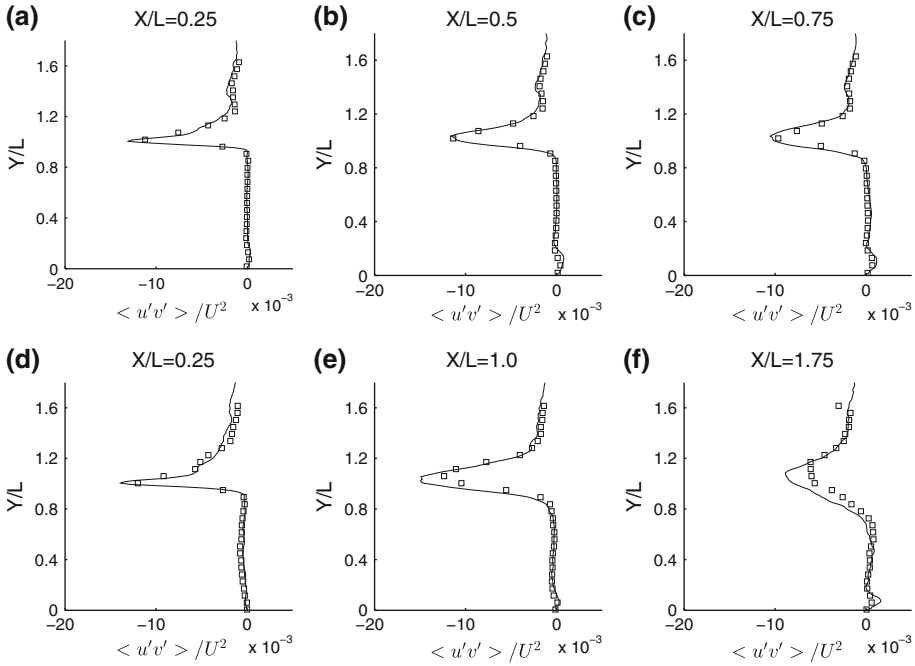

Fig. 11 Comparison between numerical results (*solid line*) and experimental measurements (*symbols*) for $\langle u'v' \rangle / U^2$ at three X/L positions. **a**–**c** $\lambda = 1$, **a** $X/L = 0.25$, **b** $X/L = 0.5$, **c** $X/L = 0.75$. **d**–**f** $\lambda = 2$, **d** $X/L = 0.25$, **e** $X/L = 1$, **f** $X/L = 1.75$.

available from the simulations is much larger than in the experiments, since whole three-dimensional fields are available. We use in the following this information to characterise the structure of the flow, disregarding the region in the lee of the upstream obstacle for case $\lambda = 2$.

4.2 Vertical structure of the flow

We start by considering the vertical structure of the flow outside of the DZ. The presence of the obstacle sequence produces a streamwise momentum deficit (see Fig. 8) which is reflected on the spanwise gradient of the transversal profile of $\langle u \rangle$. The profiles display an inflection point close to $Y/L = 1$. This deficit is also associated to changes on the vertical velocity distribution. In Fig. 12 profiles of the mean streamwise velocity as a function of Z/L at various Y/L are shown. In addition to time-average, the streamwise velocity has been averaged in streamwise direction. These streamwise-averaged profiles do not differ much from the profiles taken at a single X/L location, for example half-way between the obstacles. The profiles are shown at several locations starting from the physical interface, $Y/L = 1$ up to $Y/L = 3.5$. Near the interface $\langle u \rangle$ shows an almost uniform distribution. In the region between $Y/L = 1$ and $Y/L \sim 2$, the maximum of the velocity distribution does not occur at the water surface as in straight open channel flow. Instead, the maximum is located for the profile at $Y/L = 1.2$ roughly at half the water depth. With increasing Y the maximum is displaced towards the water surface. Beyond $Y/L \sim 2$ the standard logarithmic shape of the open channel velocity profile is recovered. The profiles of both cases $\lambda = 1$ and

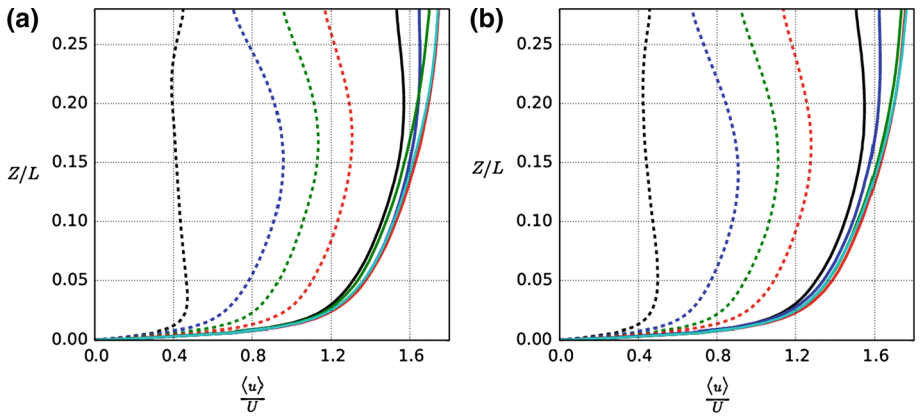

Fig. 12 Mean streamwise velocity profile as a function of the vertical coordinate Z/L at several Y/L simulation positions. In addition to the time-average, the profiles have been also averaged in streamwise direction. Line styles correspond to $Y/L = 1.0$ (*dashed black*), $Y/L = 1.2$ (*dashed blue*), $Y/L = 1.4$ (*dashed green*), $Y/L = 1.6$ (*dashed red*), $Y/L = 2.0$ (*solid black*), $Y/L = 2.15$ (*solid blue*), $Y/L = 2.5$ (*solid green*), $Y/L = 3.0$ (*solid red*), $Y/L = 3.5$ (*solid cyan*). **a** $\lambda = 1$, **b** $\lambda = 2$.

$\lambda = 2$ present similar features, indicating that the outer mean flow is not very sensitive to the spacing between obstacles.

We turn now our attention to the secondary currents present in the flow. Figures 13 and 14 show streamlines of the mean flow projected in selected transverse YZ-planes. Since streamlines are sometimes misleading because they do not represent the velocity magnitude, we have added colour-contours corresponding to the mean streamwise vorticity, $\langle \omega_x \rangle$. Therefore, secondary currents in regions of small $\langle \omega_x \rangle$ can be ignored. The analysis of the streamlines shows that a streamwise secondary current composed of two cells (2SC) is formed in the region immediately adjacent to the obstacles. For both λ, the top secondary current spans from $Y/L = 1$ until approximately $Y/L = 2$, while the bottom one spans from $Y/L = 1$ until approximately $Y/L = 1.5$. The 2SC is not vertically symmetric and its core is approximately located between $Y/L = 1.1$ and 1.2. The secondary current is therefore located in the region where the mean streamwise velocity vertical profile has a maximum away from the water surface, Fig. 12. Thus, the streamwise momentum deficit (Fig. 8) is not only due to the superposition of turbulent eddies from upstream obstacles, but also part of the energy of the flow is used to sustain the secondary current.

An additional, but smaller, secondary cell system can be also observed in Figs. 13 and 14 within the DZ, near the edge of the obstacles. The main difference between both aspect ratios, is the larger size of the current in case $\lambda = 2$. For both aspect ratios, the mean streamwise vorticity is of the order of the one associated to the external, secondary current system. For both λ, the internal secondary current system vanish in the upstream region, probably due to the DZ's advective current, which flows towards the main channel. The size of these internal secondary structures increases with the downstream direction, with a maximum size at approximately half-way between the obstacles. They finally disappear when the main stream is deflected towards the DZ in the downstream impingement region. Note that even though the presence of the system of secondary currents is not discussed in the paper of McCoy et al. [17], it is possible to identify it in the mean spanwise streamlines presented in that work. Therefore, it appears that the topology of these structures does not depend on the bathymetric conditions. Furthermore, similar near bottom secondary currents have been

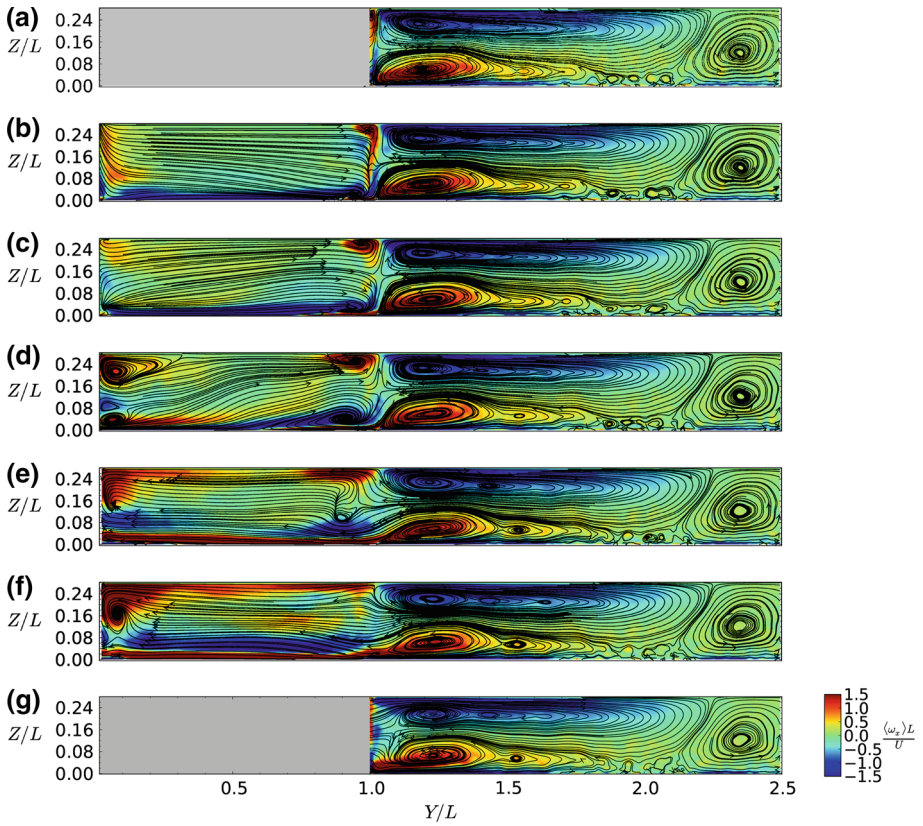

Fig. 13 Streamlines of the mean flow projected in selected Y–Z planes. Case $\lambda = 1$. *Colour* represents mean streamwise vorticity, $\langle \omega_x \rangle$. The positions of the planes are **a** $x/L = 0$, **b** $x/L = 0.1$, **c** $x/L = 0.25$, **d** $x/L = 0.5$, **e** $x/L = 0.75$, **f** $x/L = 0.9$, **g** $x/L = 1$.

identified at the interface in the work of Abad et al. [1], in groynes for control of riverbank erosion in a small non-shallow natural flow.

From the mean field results it can be observed that the exchange of fluid from main stream to DZ takes place mainly near the downstream obstacle with a clear vertical uniformity. Additional inflow occurs near the bottom over the whole streamwise length of the DZ. Horizontal streamlines in the X–Y plane (not shown) indicate that most of the mean flow leaves the DZ close to the water surface in the lee of the upstream obstacle. McCoy et al. [17] observed a somewhat different exchange flow, since they point out that inflow from the main channel to DZ mainly occured at levels situated at mid-depth. This is an indication that the exchange process between DZ and main stream might be influenced by the channel bathymetry.

Figures 15 and 16 show streamlines of the mean flow projected in selected transverse XZ-planes. Colour in this case corresponds to mean spanwise vorticity $\langle \omega_y \rangle$. Even though the analysed geometry is less shallow than previous studies [17,27], it is still possible to observe that in most of the DZ region the velocities remain relatively uniform in the vertical direction. Most of the streamlines are parallel, validating once more the vertical homogeneity of the flow pointed out previously by Sukhodolov et al. [23] and McCoy et al. [17]. This

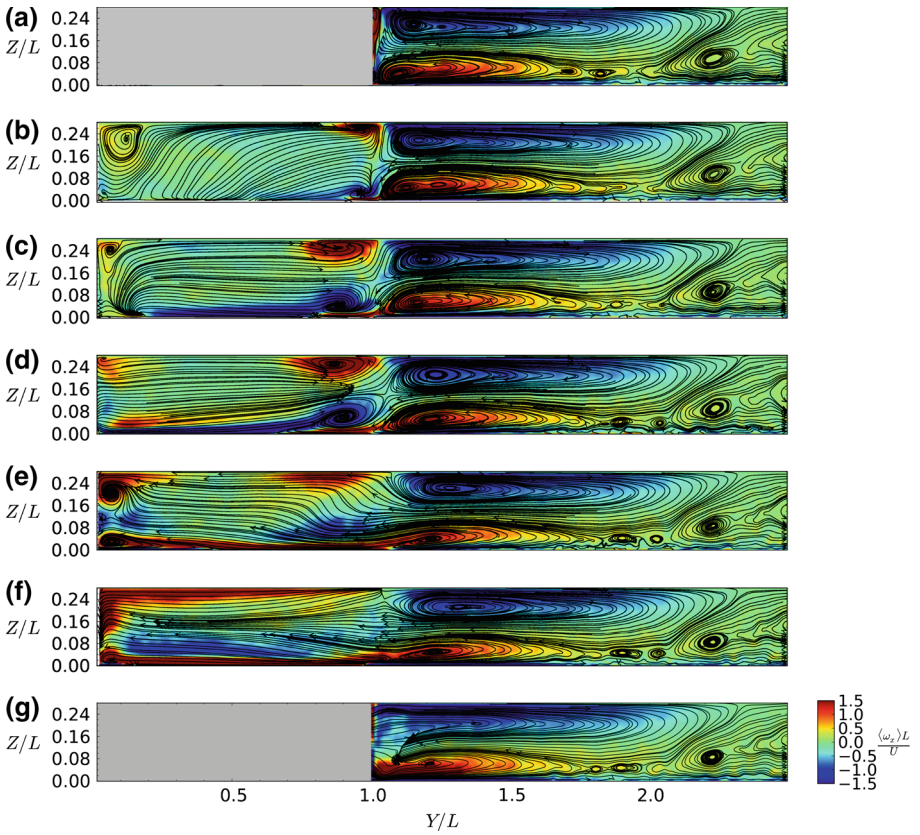

Fig. 14 Streamlines of the mean flow projected in selected Y–Z planes. Case $\lambda = 2$. *Colour* represents mean streamwise vorticity, $\langle \omega_x \rangle$. The positions of the planes are **a** $x/L = 0$, **b** $x/L = 0.2$, **c** $x/L = 0.5$, **d** $x/L = 1$, **e** $x/L = 1.5$, **f** $x/L = 1.8$, **g** $x/L = 2$.

homogeneity can be also observed in the streamlines of the mean flow projected in transverse planes shown above in Figs. 6 and 7.

An interesting feature of the flow can be also observed in Figs. 15 and 16, namely, a high level of spanwise vorticity at the impingement region. The flow structure in this zone corresponds to a double vortex system along the obstacle. The double vortex system can be also found in the experimental vertical planes reported by Brevis [3], but for obstacles with a rounded head. The vorticity level associated to these structures is, approximately, three times higher than the streamwise vorticity level of the secondary currents seen in Figs. 6 and 7.

We conclude this section by analysing the vertical structure of the second order statistics using data from the numerical simulations. Figure 17 show profiles of $\langle u'u' \rangle / U^2$, $\langle v'v' \rangle / U^2$, $\langle w'w' \rangle / U^2$ and $\langle u'v' \rangle / U^2$ as a function of Y/L, at $X/L = 0.5$ at selected heights in the range $0.1 < Z/h < 0.75$. The profiles of all quantities reveal the presence of the shear layer at the physical interface ($0.9 < Y/L < 1.2$), showing that the values in this zone remain rather constant over the whole depth. The exception is $\langle u'v' \rangle$ in case $\lambda = 2$, where some differences are clearly visible. While in the DZ the profiles collapse, in the outer region the turbulent levels vary as a function of the vertical coordinate, as expected in straight open-channel flow. Therefore, in a shallow DZ it is a reasonable assumption for turbulence modelling to assume that the turbulence does not change much with depth.

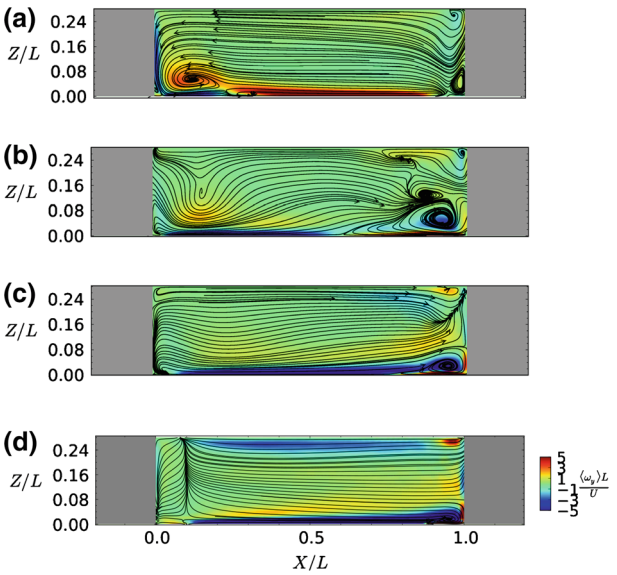

Fig. 15 Streamlines of the mean flow projected in selected X–Z planes. Case $\lambda = 1$. *Colour* represents mean spanwise vorticity, $\langle\omega_y\rangle$. The positions of the planes are **a** $y/L = 0.1$, **b** $y/L = 0.6$, **c** $y/L = 0.8$, **d** $y/L = 0.95$.

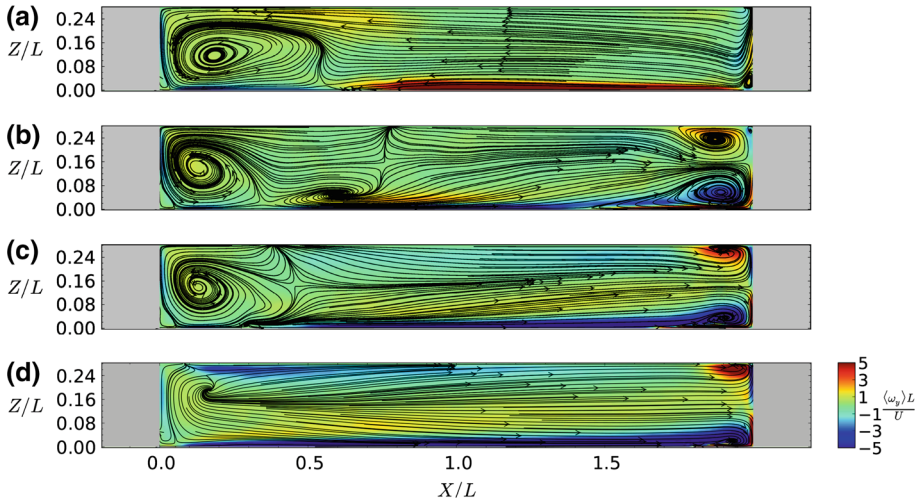

Fig. 16 Streamlines of the mean flow projected in selected X–Z planes. Case $\lambda = 2$. *Colour* represents mean spanwise vorticity, $\langle\omega_y\rangle$. The positions of the planes are **a** $y/L = 0.1$, **b** $y/L = 0.6$, **c** $y/L = 0.8$, **d** $y/L = 0.95$.

4.3 Wall shear stress

In this section we estimate the mean and rms wall shear stress for both cases $\lambda = 1$ and $\lambda = 2$. We assume that, near the wall, the vertical velocity is negligible and that the only significant variations occur for the horizontal velocity components in the bottom-wall-normal direction.

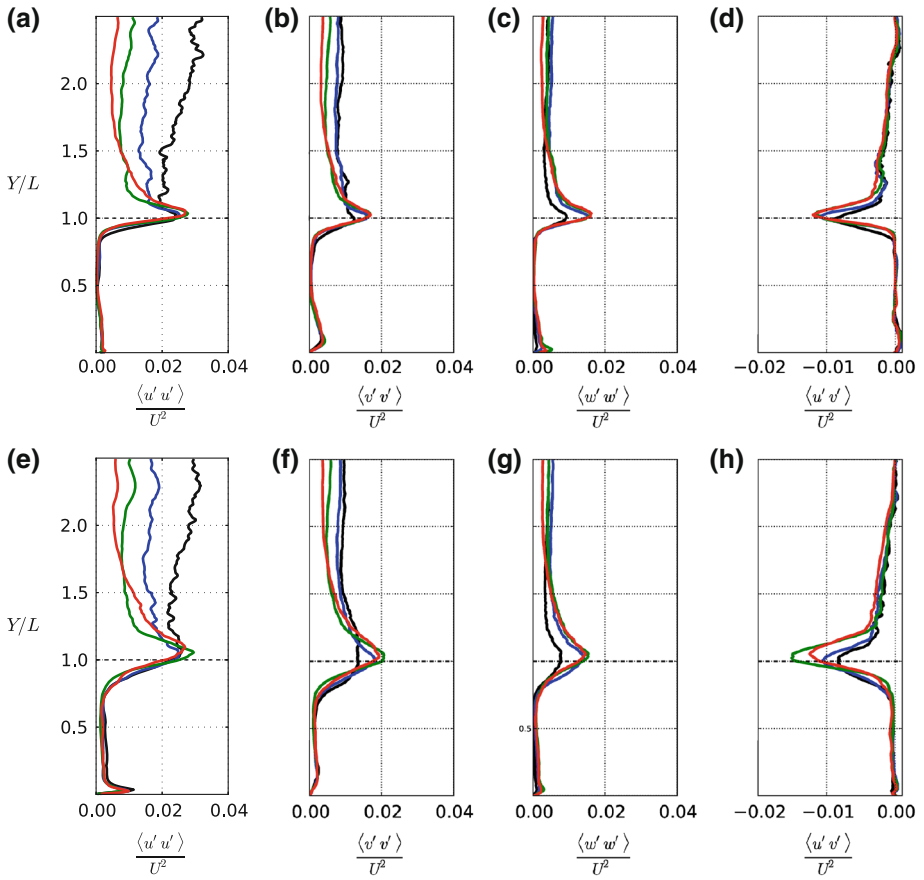

Fig. 17 Second-order statistics versus Y/L. The streamwise location corresponds to half-way between the obstacles. Line styles correspond to $Z = 0.1h$ *(black)*, $Z/L = 0.25h$ *(blue)*, $Z/L = 0.5$ *(green)*, $Z/L = 0.75$ *(red)*. **a**–**d**: $\lambda = 1$; **e**–**h**: $\lambda = 2$. **a**, **e** $\langle u'u' \rangle$, **b**, **f** $\langle v'v' \rangle$, **c**, **g** $\langle w'w' \rangle$, **d**, **h** $\langle u'v' \rangle$.

The latter is not strictly true since near the obstacles significant variations might occur in both streamwise and spanwise directions. Under this approximation, we estimate the mean and rms wall-shear stress as:

$$\langle \tau_w \rangle = \sqrt{\left(\frac{\mathrm{d}\langle u \rangle}{\mathrm{d}z}\right)^2 + \left(\frac{\mathrm{d}\langle v \rangle}{\mathrm{d}z}\right)^2} \tag{1}$$

$$\tau_w^{rms} = \sqrt{\left(\frac{\mathrm{d}u_{rms}}{\mathrm{d}z}\right)^2 + \left(\frac{\mathrm{d}v_{rms}}{\mathrm{d}z}\right)^2} \tag{2}$$

where the rms of a quantity ϕ is $\phi_{rms} = \sqrt{\langle \phi' \phi' \rangle}$.

Figures 18 and 19 show the mean and rms wall shear stress for case $\lambda = 1$ and case $\lambda = 2$ respectively, normalised by a mean reference value which is taken in the outer stream, $\tau_{ref} = \langle \tau_w \rangle (y/L = 3)$. For both λ, in the dead zone the values of $\langle \tau_w \rangle$ are small compared to the values in the mean stream, with the exception of the region near the downstream obstacle where impingement takes place.

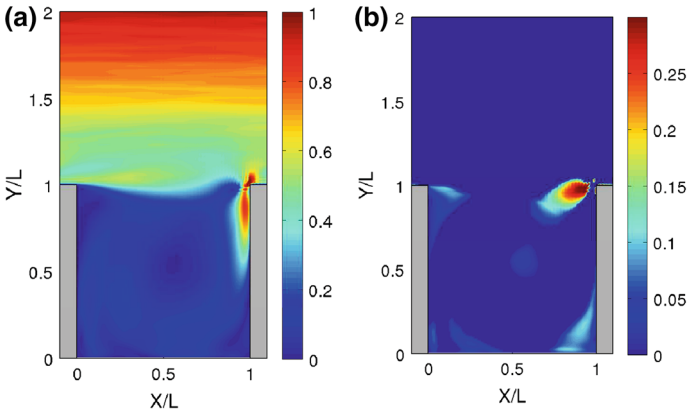

Fig. 18 Mean (**a**) and rms (**b**) wall shear stress in case $\lambda = 1$. Both normalized with the mean wall shear stress in the main channel at $y/L = 3$.

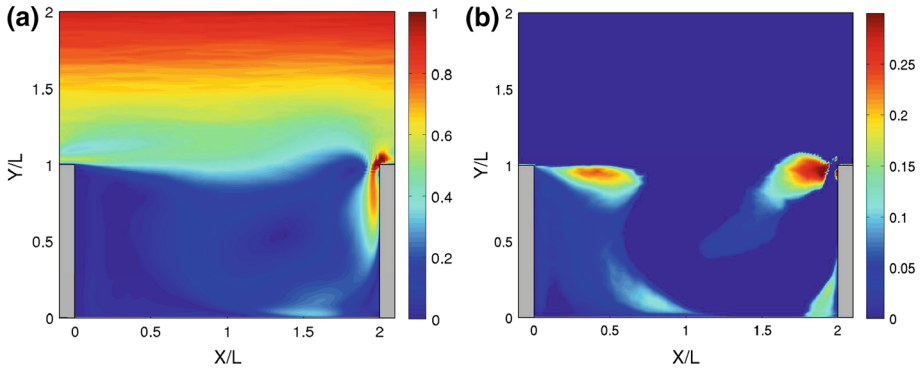

Fig. 19 Mean **a** and rms **b** wall shear stress in case $\lambda = 2$. Both normalized with the mean wall shear stress in the main channel at $y/L = 3$.

In contrast, the values of τ_w^{rms} are significantly larger in the DZ than in the main stream, reaching up to $0.3\tau_{ref}$. In case $\lambda = 1$, the region of high τ_w^{rms} is concentrated near the downstream obstacle, i.e. in the region of impingement. In case $\lambda = 2$, in addition to the impingement region, high values of τ_w^{rms} are obtained behind the downstream obstacle, near the outer edge of the DZ. A hyphotesis is that this might result from flapping motion of the nearby shear layer.

Note that even though a different geometry than the one associated to fluvial groyne fields was used in this work, it is still possible to see some correlation between both cases. The zones of bed erosion just downstream the upstream groyne observed by various authors [22,24] in groynes fields might be related with the higher bed shear stress shown, for instance, in Fig. 19*b*. According to the fluvial literature, no important erosion takes place on the upstream face of the downstream groynes, thus it may be possible that a square-geometry obstacle produces shear-stresses levels in the impingement region larger than those developed in fluvial rounded geometries.

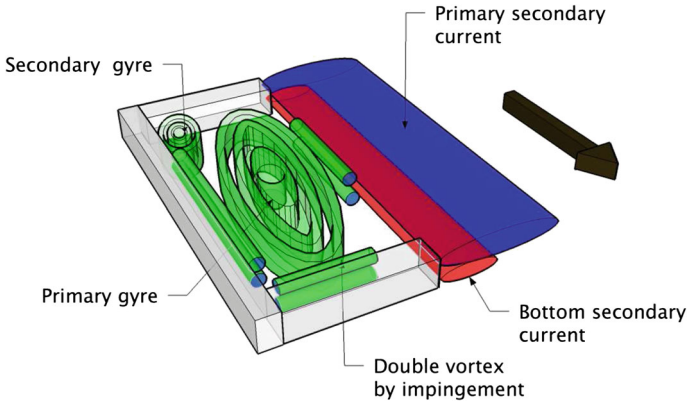

Fig. 20 Sketch of three-dimensional structure of the shallow-flow around an emerged obstacles sequence of $\lambda = 2$.

5 Conclusions

Experiments using particle image velocimetry and large eddy simulations of shallow flow around an emerged obstacles sequence have been performed. Two aspect ratios of the resulting DZs have been considered, $\lambda = 1$ and $\lambda = 2$. The comparison between experimental and numerical results have shown that both results are in good agreement for both cases. In spite of the fact that the grid resolution could have been better in some regions, the satisfactory predictions of mean and second order statistics have provided confidence in the results. Therefore, it has been possible to study the vertical structure of the flow using the data obtained from the LES. The only exception is the region in the lee of the upstream obstacle where a secondary gyre observed in the experiments has not been predicted in the simulations.

As a summary of the mean flow structures observed in the flow around an obstacles sequence, Fig. 20 provides a sketch with the present observations for case $\lambda = 2$. The case $\lambda = 1$ would be similar but without the secondary gyre in the lee of the upstream obstacle. The flow in the DZ is dominated by a large recirculation zone that occupies almost the whole DZ. In the impingement region a relatively strong, spanwise, double-vortex system is formed that might be responsible for erosion patterns in natural flows. Near the interface between DZ and main stream two streamwise double-vortex systems are present. The outer one, when superimposed to the main stream, can be interpreted as a mean helicoidal current in this zone. This helicoidal current, if it is also formed in natural flows, can influence the dynamic of sediment transport.

Concerning the differences between the two aspect ratios considered, it has been shown that the outer flow is not very sensitive to this parameter. In particular very similar turbulence levels have been obtained in both cases in the outer zone. For the flow within the DZ, on the other hand, some important differences have been observed. For $\lambda = 2$, the interfacial shear layer has more length to develop. This leads to a thicker shear layer near the downstream obstacle and indirectly to a higher level of turbulence within the DZ. For $\lambda = 1$, the latter has shown to be almost negligible within the DZ. Another important difference appears for the wall-shear stress. Values of mean wall shear-stress for both cases are small in the DZ as compared the values in the main stream. However, values of the rms wall shear-stress are large within the DZ compared to the main stream. This is particularly true for case $\lambda = 2$,

where high values are observed in the lee of the upstream obstacle. In this region high levels of bed erosion have been observed in natural flows.

References

1. Abad JD, Rhoads BL, Guneralp I, Garcia MH (2008) Flow structure at different stages in a meander-bend with bendway weirs. J Hydraul Eng 134(8):1052–1063
2. Breuer M, Rodi W (1996) large eddy simulation of complex turbulent flows of practical interest. In: Hirschel E (ed) Flow simulation with high performance computers II, notes on numerical fluid mechanics, vol 52. Vieweg, Braunschweig, pp 258–274
3. Brevis W (2009) Experimental investigation of the flow hydrodynamics in open-channel dead zones. PhD thesis, Faculty of Physical and Mathematical Sciences, University of Chile
4. Brevis W, García-Villalba M (2011) Shallow-flow visualization analysis by proper orthogonal decomposition. J Hydraul Res 49(5):586–594
5. Brevis W, Niño Y, Jirka G (2010) Integrating cross-correlation and relaxation algorithms for particle tracking velocimetry. Exp Fluids 50(1):135–147
6. Constantinescu G, Sukhodolov A, McCoy A (2009) Mass exchange in a shallow channel flow with a series of groynes: les study and comparison with laboratory and field experiments. Environ Fluid Mech 9(6):587–615
7. García-Villalba M, Fröhlich J, Rodi W (2006) Identification and analysis of coherent structures in the near field of a turbulent unconfined annular swirling jet using large eddy simulation. Phys Fluids 18(055):103
8. García-Villalba M, Li N, Rodi W, Leschziner MA (2009) large eddy simulation of separated flow over a three-dimensional axisymmetric hill. J Fluid Mech 627:55–96
9. Germano M, Piomelli U, Moin P, Cabot W (1991) A dynamic subgrid-scale eddy viscosity model. Phys Fluids 3:1760–1765
10. Hankin B, Holland M, Beven K, Carling P (2002) Computational fluid dynamics modelling of flow and energy fluxes for a natural fluvial dead zone. J Hydraul Res 40:389–400
11. Hinterberger C (2004) Dreidimensionale und tiefengemittelte large-eddy-simulation von Flachwasserströmungen. PhD thesis, University of Karlsruhe
12. Hinterberger C, Fröhlich J, Rodi W (2007) Three-dimensional and depth-averaged large-eddy simulations of some shallow water flows. J Hydraul Eng 133:857
13. Jacoub G, Westrich B (2006) Effect of river groyne structures on flow, sedimentation and erosion dynamics in rivers (Case study: the River Elbe). Geophys Res Abstr 8(06):315
14. Karami H, Basser H, Ardeshir A (2012) Verification of numerical study of scour around spur dikes using experimental data. Water Environ J
15. Kirkgöz M, Ardiclioglu M (1997) Velocity profiles of developing and developed open channel flow. J Hydraul Eng 123:1099
16. Lilly D (1992) A proposed modification of the Germano subgrid-scale closure method. Phys Fluids 4:633–635
17. McCoy A, Constantinescu G, ASCE M, Weber L (2008) Numerical Investigation of Flow Hydrodynamics in a Channel with a Series of Groynes. J Hydraul Eng 134:157
18. Nezu I, Rodi W (1985) Experimental study on secondary currents in open channel flow. In: Proceedings of 21st IAHR Congress, vol 2
19. Palau-Salvador G, García-Villalba M, Rodi W (2011) Scalar transport from point sources in the flow around a finite-height cylinder. Environ Fluid Mech 11(6):611–625
20. Scarano F (2002) Iterative image deformation methods in piv. Meas Sci Technol 13:R1
21. Schiemer F, Hein T (2007) The ecological significance of hydraulic retention zones. Hydroecol Ecohydrol 14:405–420
22. Sukhodolov A, Uijttewaal W, Engelhardt C (2002) On the correspondence between morphological and hydrodynamical patterns of groyne fields. Earth Surf Process Landf 27(3):289–305
23. Sukhodolov A, Engelhardt C, Krüger A, Bungartz H (2004) Case study: turbulent flow and sediment distributions in a groyne field. J Hydraul Eng 130:1
24. Ten Brinke W, Schulze FH, van Der Veer P (2004) Sand exchange between groynefield beaches and the navigation channel of the Dutch Rhine: the impact of navigation versus river flow. River Res Appl 20(8):899–928
25. Tritthart M, Liedermann M, Habersack H (2009) Modelling spatiotemporal flow characteristics in groyne fields. River Res Appl 25(1):62–81

26. Uijttewaa W, Lehmann D, Mazijk A (2001) Exchange process between a river and its groyne fields: model experimets. J Hydraul Eng 127:928–936
27. Weitbrecht V (2004) Influence of dead-water zones on dispersive mass transport in rivers. PhD thesis, University of Karlsruhe, Institut for Hydrodynamics
28. Weitbrecht V, Socolofsky S, ASCE M, Jirka G, ASCE F (2008a) Experiments on mass exchange between groin fields and main stream in rivers. J Hydraul Eng 134:173
29. Weitbrecht V, Socolofsky SA, Jirka GH (2008b) Experiments on mass exchange between groin fields and main stream in rivers. J Hydraul Eng 134(2):173–183
30. Westerweel J, Scarano F (2005) Universal outlier detection for piv data. Exp Fluids 39(6):1096–1100